ACS APPLIED ENERGY MATERIALS

Article

Unlocking the Potential of Fluoride-based Solid Electrolytes for Solid-State Lithium Batteries

Max Feinauer, Holger Euchner, Maximilian Fichtner, and M. Anji Reddy

ACS Appl. Energy Mater., **Just Accepted Manuscript** • DOI: 10.1021/acsaem.9b01166 • Publication Date (Web): 09 Sep 2019

Unlocking the Potential of Fluoride-based Solid Electrolytes for Solid-State Lithium Batteries

*Max Feinauer [a], Holger Euchner [a], Maximilian Fichtner [a, b], M. Anji Reddy [a, *]*

[a] Helmholtz Institute Ulm (HIU) Electrochemical Energy Storage, Helmholtzstr.11, 89081 Ulm, Germany

[b] Karlsruhe Institute of Technology, Institute of Nanotechnology, Hermann-von-Helmholtz-Platz 1, 76344 Eggenstein-Leopoldshafen, Germany

*Corresponding author Email: munnangi.reddy@kit.edu

Abstract

The development of high energy density and sustainable all-solid-state lithium batteries relies on the development of suitable Li^+ transporting solid electrolytes with high chemical and electrochemical stability, good interfacial compatibility, and high ionic conductivity. Ceramic-based electrolytes show high bulk Li^+ conductivity and stability but exhibit poor mechanical properties. In contrast, few sulfide-based electrolytes show high total Li^+ conductivity and better mechanical properties but poor chemical and electrochemical stability. Moreover, both types of electrolytes exhibit interfacial compatibility issues with several electrode materials. Here, we reveal the potential of Li-containing metal fluorides as Li^+ conducting solid electrolytes for solid-state lithium batteries, demonstrating their viability with a case study on β-Li_3AlF_6. We have synthesized β-Li_3AlF_6 by mechanical milling and investigated its properties as a solid electrolyte. Ionic conductivity of 3.9×10^{-6} S cm^{-1} was observed at 100 °C, which was increased to 1.8×10^{-5} S cm^{-1} by compositing with nanocrystalline alumina (γ-Al_2O_3). Furthermore, the performance of β-Li_3AlF_6 as a solid electrolyte was successfully tested in an all-solid-state lithium battery using $LiMn_2O_4$ as cathode and Li metal as an anode. Finally, we have used density functional theory to shed light on the Li diffusion pathways and associated activation barriers in β-Li_3AlF_6. Overall, our studies reveal the hidden potential of Li-containing metal fluorides as solid electrolytes for all-solid-state lithium batteries.

Keywords: *Solid-state lithium batteries; Solid electrolytes; Fluoride-based electrolyte; Li-ion conductors; Li_3AlF_6;*

Introduction

Lithium-ion batteries (LIBs) use liquid electrolytes (LEs), which poses severe safety concerns due to the flammability of the latter ones. Also, Li metal anodes, which offer the desired high capacities form dendrites in LEs, which eventually leads to short-circuit and causes the breakdown of the cell [1]. To avoid the issues associated with Li metal, it was replaced with graphite in commercial LIBs, though the capacity of graphite is ten times lower than that of Li metal [1]. Employing graphite as an anode demands the use of lithiated cathode materials (e.g., $LiCoO_2$ or $LiFePO_4$). On the other hand, Li metal as an anode facilitates the use of unlithiated compounds and therefore widens the choice of cathode materials. This allows the use of high-energy cathode materials that are essentially free of undesired cobalt. For example, sulfur (S) could be used as cathode material (specific energy of S is ~ 3685 Wh kg^{-1}). Under this scenario, solid electrolytes (SEs) exhibit several advantages: SEs suppress Li dendrite formation, thus enabling the use of high capacity Li metal as an anode. Moreover, SEs are non-flammable and prevent chemical crossover. More importantly, SEs show high Li^+ transport numbers which enables high power density for solid-state batteries (SSBs) [2-4]. Despite the apparent advantages offered by SS-LBs, their use is currently limited by the availability of suitable Li^+ transporting SEs [5].

Numerous Li^+ transporting SEs have been reported with high ionic conductivities, in principle providing the possibility to build SS-LBs. Beyond solid polymer electrolytes, Li^+ transporting SEs can be broadly categorized into ceramic and sulfide-based electrolytes. Several review articles dealt with different aspects of these solid electrolytes [6-10]. Briefly, ceramic electrolytes based on NASICON, perovskite, and garnet-type structures show high bulk Li^+ conductivity and stability, but are, due to their high mechanical rigidity, difficult to integrate into all-solid-state batteries. In contrast, sulfide-based electrolytes show high total Li^+ conductivity and are, due to their excellent

mechanical properties, relatively easy to integrate into all-solid-state batteries. However, they suffer from low electrochemical stability. More importantly, interfacial issues persist with both types of electrolytes [5, 11]. Richards *et al*. predicted the electrochemical and interfacial stability of various Li^+ transporting SEs with state-of-the-art cathode materials and Li metal [5]. They found that many highly conducting SEs exhibit either low interfacial or electrochemical stability. Interestingly, their results show high interfacial and electrochemical stability for fluoride-based Li^+ transporting SEs [5].

Unique features of fluoride-based solid electrolytes: Fluorine has a high formation potential (+2.87 V/SHE), even compared to the oxygen evolution potential (+1.23 V/SHE), which is the origin of electrochemical stability found in fluoride-based electrolytes. Furthermore, the charge to size ratio of fluoride ions is 0.75, while it amounts to 1.45 for oxide ions, thus minimizing the interfacial mixing of metal fluoride based electrolytes with oxide based electrodes and improving the interfacial compatibility. Intrinsically, metal fluorides are electrical insulators, a highly desirable property for electrolyte applications. Even insertion of Li into metal fluorides does not lead to significant electronic conductivity, in contrast to lithium lanthanum titanate (LLTO) and lithium aluminum titanium phosphate (LATP) based electrolytes [12,13]. More importantly, similar to sulfide-based electrolytes, metal fluorides show excellent mechanical properties, which enable easy fabrication of all-solid-state batteries. Also, metal fluorides can be easily synthesized by mechanical milling, chemical methods, and are, moreover, facile to fabricate in the form of thin and thick films [14-20]. Conclusively, Li-containing metal fluorides possess high chemical and electrochemical stability like ceramic electrolytes and excellent mechanical properties like sulfide-based electrolytes. Apparently, fluoride-based Li^+ conducting SEs would be a *real* option for building SS-LBs. However, the major drawback of metal fluorides at this stage (which is not conclusive as the number of studies on the Li^+ conducting metal fluorides is limited) appears to be their low ionic conductivity, which, however, can be alleviated using various strategies [15,16, 21,22].

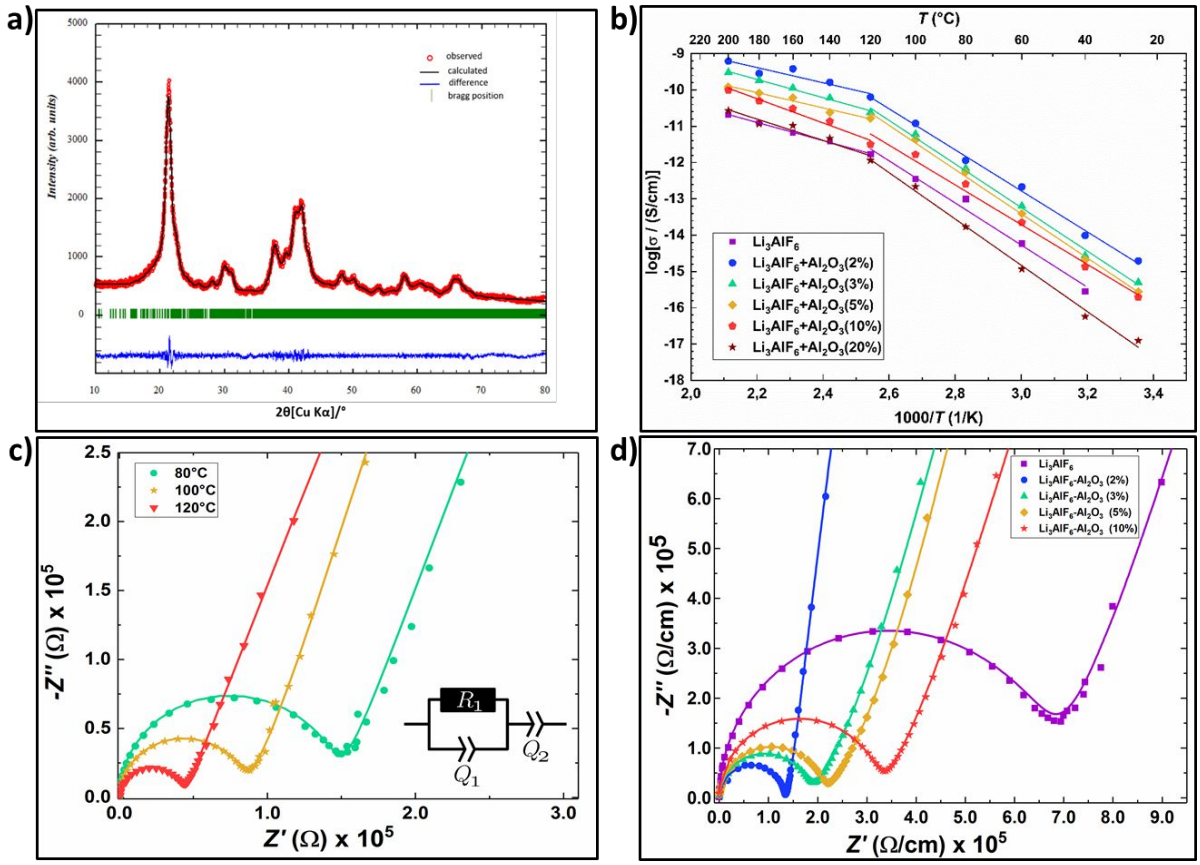

Figure 1*a) XRD pattern of as-synthesized β-Li_3AlF_6 b) Arrhenius plot for the ionic conductivity of β-Li_3AlF_6 and β-Li_3AlF_6+Al_2O_3 composites measured in the temperature range of 25 to 200 °C, c) impedance spectra of β-Li_3AlF_6 obtained at various temperatures, d) impedance spectra of β-Li_3AlF_6+Al_2O_3 composites obtained at 100 °C*

While the high ionic conductivity of the SEs is an essential criterion for the successful operation of a solid-state battery, it is the thickness (thereby area specific resistance (ASR)) of the solid electrolyte layer that is the most relevant quantity. For example, lithium phosphorous oxynitride (LiPON) with a room temperature (RT) conductivity in the order of ~10^{-6} S cm^{-1} has long been used as a solid electrolyte in thin film LIBs. Dudney *et al*. investigated solid-state thin film lithium batteries built with $LiMn_{1.5}Ni_{0.5}O_4$ cathode, LIPON electrolyte, and Li metal anode [23]. They have also built a non-aqueous lithium-ion battery with the same electrode combinations for comparison. In the case of liquid and solid-state cells, the initial ASR was 28 and 200 Ω cm^2, respectively. Despite the high ASR, the solid-state cell displayed long cycling stability (10 000 cycles). These results demonstrate that a high ASR value is tolerable in solid-state batteries as long as a thin layer of SE is used. Considering the desired thickness of 10 μm for the SE film, ionic conductivity in the range of 10^{-4} to 10^{-5} S cm^{-1} at RT would be adequate to build all-solid-state batteries. For instance, the ASR of a 10 μm thick SE film with an ionic conductivity of 10^{-5} S cm^{-1} amounts to 100 Ω cm^2, which is acceptable.

Very few Li-containing metal fluorides have been investigated for Li-ion conductivity. $LiAlF_4$ with an ionic conductivity of 1.0x10^{-6} S cm^{-1} at 25 °C is one of them [20]. So far, $LiAlF_4$ could be synthesized only in the form of amorphous thin films [24]. The compound did not even crystallize after sintering at 600 °C, indicating that it may not be stable in the crystalline form [24]. Esaka *et al*. measured the ionic conductivity of β-Li_3AlF_6, which was found to be 1.0x10^{-6} S cm^{-1} at 200 °C [25]. On the other hand, an ionic conductivity of 4x10^{-4} S cm^{-1} was observed for Si or Ti-doped β-Li_3AlF_6 at 300 °C [25]. Later, Miyazakiz and Maekawa showed that the ionic conductivity of β-Li_3AlF_6 could be increased by reducing the particle size via mechanical milling. At RT, the conductivity of nanocrystalline β-Li_3AlF_6 amounted to 7x10^{-7} S cm^{-1} and further increased to 2x10^{-6} S cm^{-1} by compositing with LiCl via mechanical milling [26]. Thus, the increase in ionic conductivity was ~1000 times as compared to microcrystalline β-Li_3AlF_6. To the best of our knowledge, so far only these two metal fluorides ($LiAlF_4$ and Li_3AlF_6) have been reported for their Li-ion conductivity. In this proof-of-concept paper, we investigated the ionic conductivity, electrochemical stability window, Li deposition, and stripping and finally validated the performance of nanocrystalline β-Li_3AlF_6 as a solid electrolyte in all solid-state lithium battery with $LiMn_2O_4$ cathode and Li metal as the anode.

Results and discussion

Li_3AlF_6 can be synthesized in five different modifications (α, β, γ, δ, and ε) by adopting various synthesis conditions [27]. The monoclinic β-modification can be obtained by slow cooling from above 600 °C, whereas fast quenching results in the α-modification [28]. Here, we have synthesized β-Li_3AlF_6 directly via mechanical milling of LiF and AlF_3 for 20 h at 600 rpm (further experimental details are given in the methods section). Fig. 1a shows the XRD pattern of the as-synthesized material. All peaks could be indexed to the β-Li_3AlF_6 phase. The average crystallite size of as-synthesized β-Li_3AlF_6 was estimated to be 20 nm as calculated from the Scherrer equation with a primary particle size in the range of 1-3 μm (Fig. S1 shows the SEM image of the as-synthesized β-Li_3AlF_6). Fig. 1b shows the Arrhenius plot for the ionic conductivity of β-Li_3AlF_6 with various doping concentrations as obtained via electrochemical impedance spectroscopy (EIS) in a temperature range of 25 to 200 °C. The corresponding impedance spectra of β-Li_3AlF_6 obtained at various temperatures and for different doping concentrations are depicted in Fig 1c and d. At RT and 100 °C the ionic conductivity of nanocrystalline β-Li_3AlF_6 amounts to 4.4x10^{-8} and 3.9x10^{-6} S cm^{-1}, respectively. Arrhenius plot of nanocrystalline β-Li_3AlF_6 shows a non-linear behavior with two regimes, differing by their respective slopes. The first regime is between RT and 120 °C, and the second slope is observed between 120 °C and 200 °C. The activation energies corresponding to these two regimes are 0.53 eV and 0.25 eV. Miyazakiz and Maekawa also observed non-linear behavior for an Arrhenius plot of nanocrystalline β-Li_3AlF_6, but they found a linear behavior for micro-sized β-Li_3AlF_6. The non-linear behavior in the ionic conduction of nanocrystalline β-Li_3AlF_6 was attributed to the annealing of crystallites above 120 °C based on differential scanning calorimetry (DSC) [26].

The low ionic conductivity of β-Li_3AlF_6 might be due to the full occupancy of the Li sites since Li vacancies are necessary to get high ionic conductivity. Hence, we attempted to increase the ionic conductivity of β-Li_3AlF_6 via heterogeneous doping. The advantages of heterogeneous doping are twofold: it is expected to improve the ionic conductivity and also reduces the interfacial resistance of Li_3AlF_6 with Li metal. For instance, atomic layer deposition (ALD) of Al_2O_3 on garnet-type electrolyte

has been shown to significantly reduce the interfacial resistance of the SE with Li metal [29]. Liang studied the electrical properties of the two-phase system LiI-Al_2O_3 and found that the ionic conductivity increased significantly as compared to the pure phases [21]. Similarly, the fluoride ion conductivity of CaF_2 was increased by activation of grain boundary via Lewis acids (SbF_5 or BF_3) [22]. The dispersion of the second phase, which has a chemical affinity to the mobile ion on the surface of ionic conducting solids, absorbs the mobile cation and increases the defect concentration, thereby improving the ionic conductivity. However, the absorption of mobile ions will only increase the concentration of defects, and to get significantly high ionic conductivity, the mobility of these defects still needs to be high, which depends on crystal structure and composition. Here, we used a similar strategy to increase the ionic conductivity of β-Li_3AlF_6 by compositing with Al_2O_3, where Al_2O_3 was chosen based on earlier studies [30]. Furthermore, we have selected nanocrystalline γ-Al_2O_3 to get a high surface-to-volume ratio. According to theoretical studies of Jung et al., the formation of the energetically favorable $Li_{3.4}Al_2O_3$ is expected when Al_2O_3 coating layers are deposited on Li-ion battery electrode materials [30]. To find the optimum content of Al_2O_3, we synthesized β-Li_3AlF_6+Al_2O_3 composites with varying amounts of Al_2O_3.

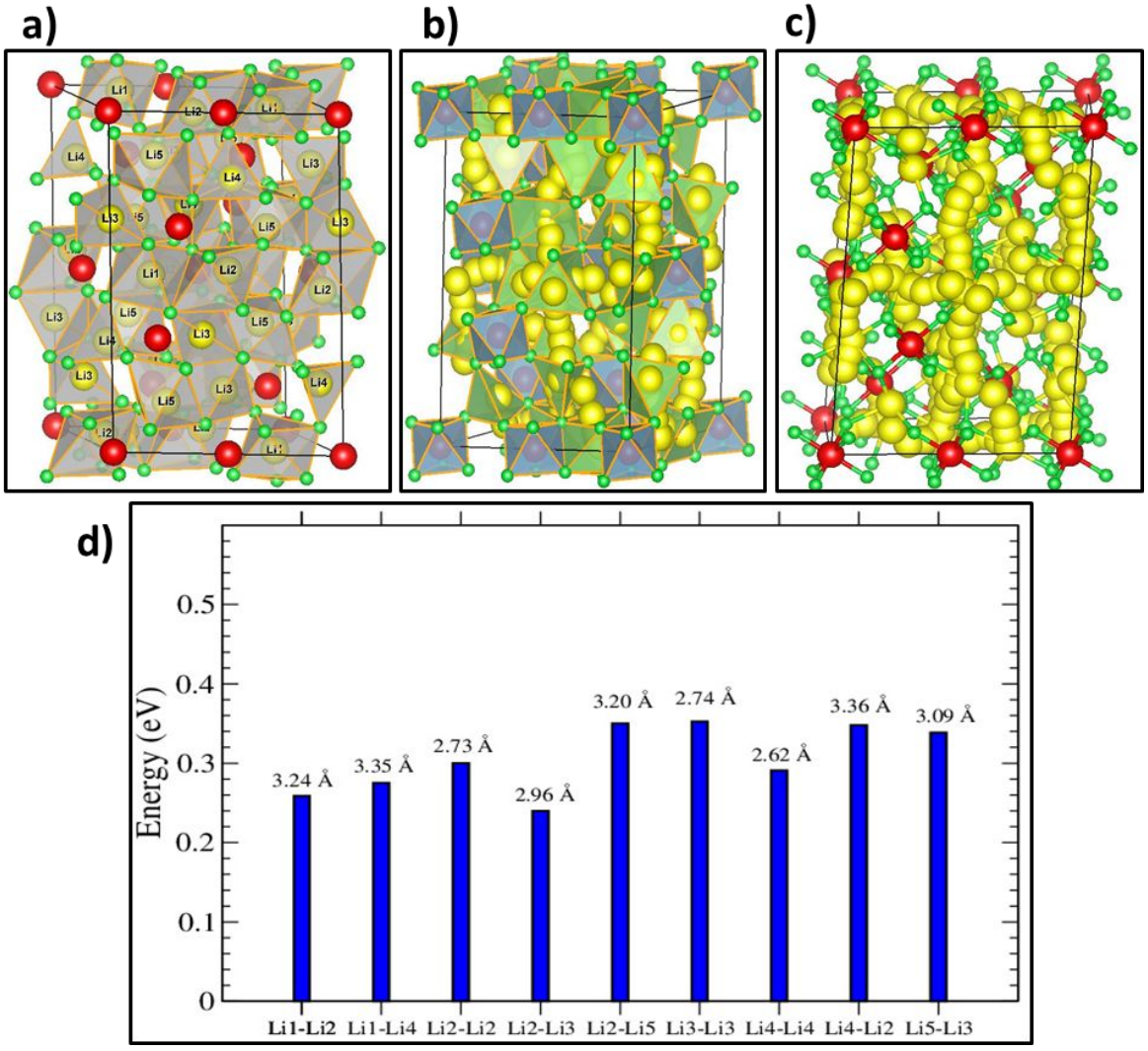

Figure 2*a) crystal structure of β-Li_3AlF_6 and (b, c) diffusion paths of Li in β-Li_3AlF_6. Li atoms are depicted in yellow, while Al and F are shown in red and green, respectively. In d) the associated Li diffusion barriers are given, also indicating the distance between the initial and final position of Li for the corresponding diffusion channel.*

Fig. S2 shows the XRD patterns of the β-Li_3AlF_6+Al_2O_3 composites. Only peaks corresponding to β-Li_3AlF_6 and γ-Al_2O_3 were observed in the XRD patterns of the composites, suggesting that indeed no new crystalline intermediate phases were formed during the synthesis of the composites. Fig. S3a

shows the scanning electron microscopic (SEM) images of the β-Li_3AlF_6+Al_2O_3 (10 wt %) composite. The elemental mappings of the corresponding SEM images are shown in Fig. S3 (b, c, d). Fluorine and oxygen were observed to be equally dispersed throughout the inspected area, suggesting a uniform distribution of Li_3AlF_6 and Al_2O_3. The EIS spectra of β-Li_3AlF_6+Al_2O_3 composites are shown in Fig. 1d. The impedance of β-Li_3AlF_6 was clearly reduced after compositing with Al_2O_3. The ionic conductivity of β-Li_3AlF_6 increased with the Al_2O_3 content up to 2 wt % and then decreased with the further addition of Al_2O_3 (conductivity values are given in Table S1). The composites with 2 wt % Al_2O_3 showed a maximum conductivity of $4.1x10^{-7}$ S cm^{-1} and $1.8x10^{-5}$ S cm^{-1} at RT and 100 °C, respectively. The ionic conductivity of the composite increased almost by a factor of ten as compared to pure β-Li_3AlF_6. The decrease in ionic conductivity with higher Al_2O_3 content could be due to the blocking effect of excess Al_2O_3. We have calculated the capacitance values associated with the semicircles (the values are given in Table S2). The capacitance lies in the range of 10^{-9} to 10^{-10} F. Such high values point at a conduction mechanism that is dominated by grain boundary diffusion [15].

To further understand the Li-ion conduction mechanism in β-Li_3AlF_6 we have applied density functional theory (DFT) to calculate the diffusion barriers associated with different Li diffusion pathways. Fig. 2a shows the crystal structure of β-Li_3AlF_6, which is built up of isolated AlF_6 octahedra, leaving wide space in which the Li-ions are located. There are five crystallographically different Li sites in distorted tetrahedral, square pyramidal and octahedral coordination. The diffusion pathways of Li in β-Li_3AlF_6 are calculated assuming that diffusion only occurs between neighboring sites. Therefore, only Li-Li distances smaller than 3.5 Å have been investigated. The resulting diffusion pathways are depicted in Fig. 2 (b, c), while the corresponding diffusion barriers are shown in Fig. 2d. Most of the diffusion barriers are well below 0.4 eV, some even falling below 0.3 eV, and the pathways form a percolating network throughout the crystal structure. The calculated activation barriers fall in the same range as the experimentally observed ones. Theoretically, we can only calculate the diffusion barriers associated with Li jumps within the crystal structure (bulk transport). However, experimentally the total activation barrier is measured which is associated with intra-grain and inter-grain diffusion of Li ions. Therefore, it is inadequate to directly compare the activation barriers that are measured experimentally and theoretically. Nevertheless, it should be noted that the computed barriers are reasonably low to allow for bulk Li diffusion through thin electrolyte films.

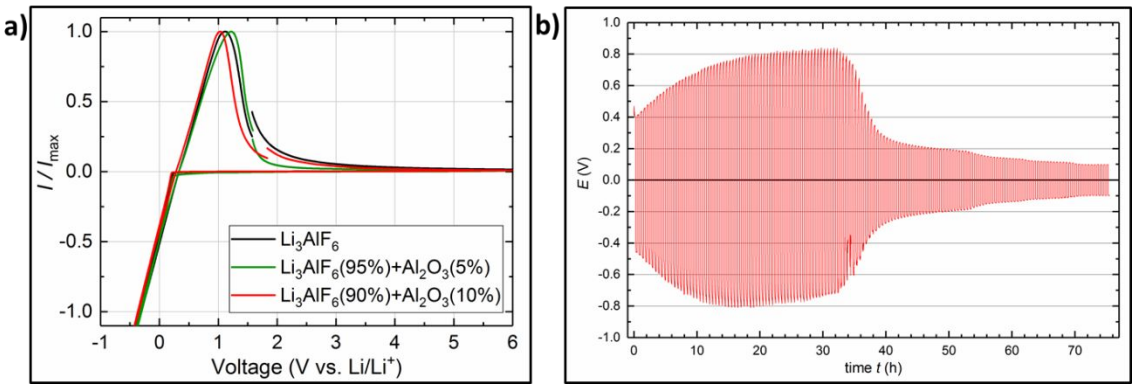

Figure 3*a) cyclic voltammogram of Li/β-Li_3AlF_6/Al and Li/ β-Li_3AlF_6+Al_2O_3/Al cells obtained at 100 °C in the voltage window of -0.5 to 6.0 V (normalized) and b) chronopotentiometry of a Li/β-Li_3AlF_6/Li cell at 100 °C.*

Cyclic voltammograms (CVs) of β-Li_3AlF_6 and β-Li_3AlF_6+Al_2O_3 composites are shown in Fig. 3a. In addition, CVs corresponding to the first 10 cycles are given in Fig. S4. For the CV measurements, β-Li_3AlF_6 or β-Li_3AlF_6+Al_2O_3 was pressed between Li and Al foil and scanned in the voltage window of -0.5-6.0 V at 100 °C. The voltage scan rate used for CV measurements was 1 mV s^{-1}. Both cathodic and anodic peaks are observed in the CV, resulting from Li deposition and stripping. Both β-Li_3AlF_6 and the β-Li_3AlF_6+Al_2O_3 composites were found to be stable up to 6.0 V. Further, chronopotentiometry (CP) measurements were performed on symmetric Li/β-Li_3AlF_6/Li cells to evaluate the deposition and stripping characteristics of β-Li_3AlF_6 (Fig.3b). Initially, Li deposition/stripping occurred at around ±0.4 V, then gradually increased to ±0.8 V and finally decreased to ±0.1 V. The reasons for the initial increase of deposition/stripping potentials are not clear

at this stage. The decrease of the deposition/stripping voltage in subsequent cycles might, on the other hand, be due to the gradual formation of a LiAl alloy at the interface between Li metal and Li_3AlF_6. The thermodynamic reduction potential of β-Li_3AlF_6 and the formation of LiAl are 1.03 V and 0.36 V vs. Li^+/Li, respectively. Therefore, the direct contact between Li and β-Li_3AlF_6 should initially lead to the formation of Al and LiF, which subsequently reacts with Li and forms a LiAl alloy at the interface according to the following equations.

β-Li_3AlF_6 + 3Li → 6LiF + Al

Al + Li → LiAl

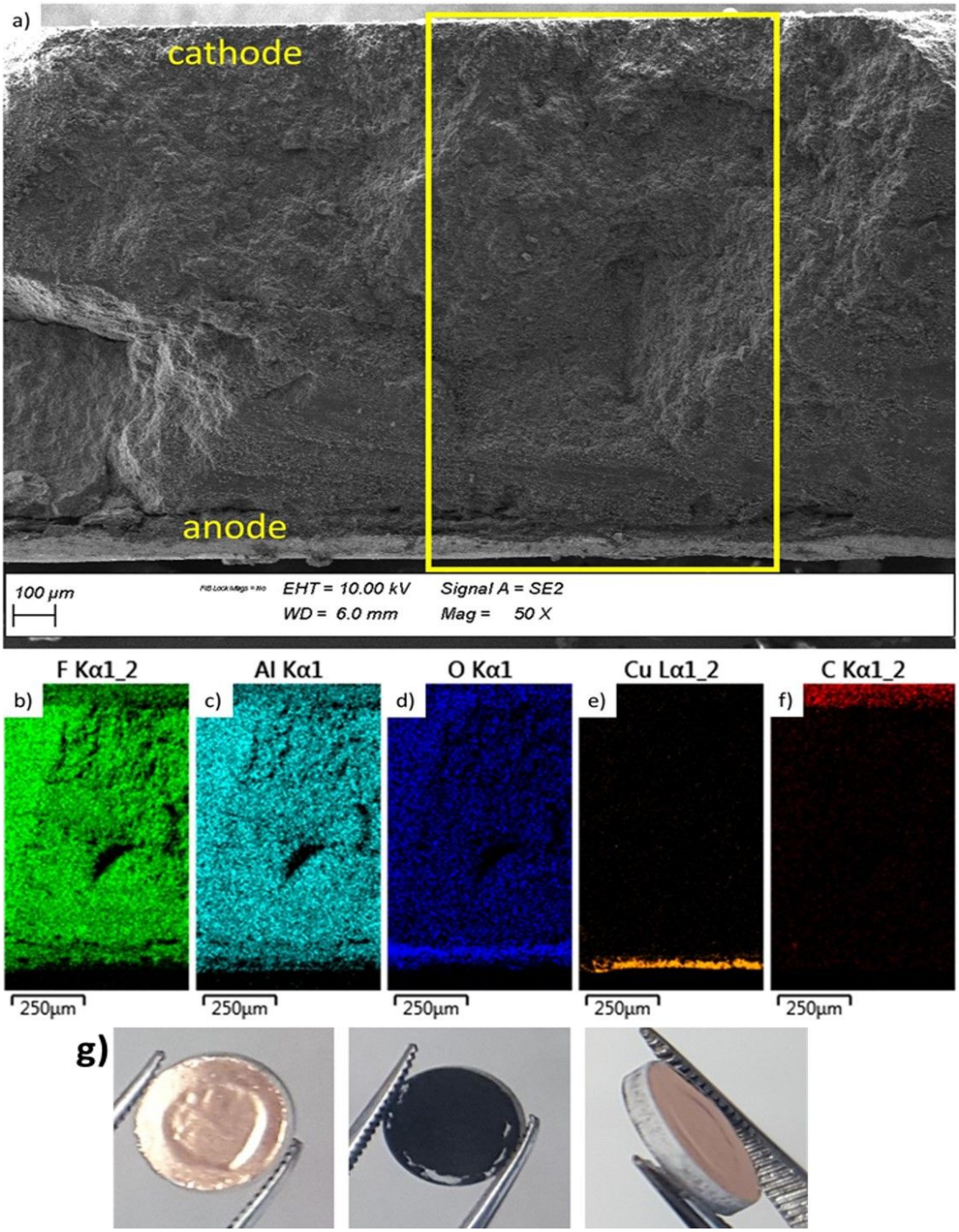

Figure 4 *a) cross-sectional SEM image of $LiMn_2O_4$/β-Li_3AlF_6/Li (Cu) pellet, corresponding (b, c, d, e, f) elemental mapping and (g) digital photos of the pellet (7 mm diameter, ~1mm thick)*

Finally, we have validated β-Li_3AlF_6 and β-Li_3AlF_6+Al_2O_3 as solid electrolytes in all-solid-state batteries using $LiMn_2O_4$ composite as cathode and Li metal as the anode. For this purpose, $LiMn_2O_4$ was synthesized by solid-state reaction. As-synthesized $LiMn_2O_4$ was mechanically milled with electrolyte and carbon to enable electronic and ionic transport within the composite. The XRD patterns of as-synthesized $LiMn_2O_4$, β-Li_3AlF_6 and $LiMn_2O_4$+β-Li_3AlF_6+C (40 wt % + 50 wt % + 10 wt %) composites are shown in Fig. S5. They only consist of peaks that are due to $LiMn_2O_4$ and β-Li_3AlF_6. In the XRD patterns of the $LiMn_2O_4$+β-Li_3AlF_6+C composite, the observed peaks correspond to $LiMn_2O_4$, β-Li_3AlF_6 and γ-Al_2O_3, suggesting that no new crystalline intermediate phases are formed during the preparation of the composite. Fig. S6 (a, b, c, d) shows the SEM images of $LiMn_2O_4$, $LiMn_2O_4$+β-Li_3AlF_6, $LiMn_2O_4$+β-Li_3AlF_6+Al_2O_3(5%), $LiMn_2O_4$+β-Li_3AlF_6+Al_2O_3(10%) composites, respectively. These images reveal a good mixing of electrode and electrolyte particles. Fig. S7 shows the SEM image and corresponding EDX mapping of $LiMn_2O_4$+β-Li_3AlF_6+Al_2O_3+C composites. The EDX mapping reveals the uniform distribution of Mn, Al, F, O, and C. All solid-state batteries were assembled by sandwiching β-Li_3AlF_6 or β-Li_3AlF_6+Al_2O_3 solid electrolyte between $LiMn_2O_4$ composite cathode and Li anode. Fig. 4a shows the cross-sectional SEM image of a $LiMn_2O_4$/β-Li_3AlF_6/Li (Cu) pellet and corresponding elemental mapping of F (b), Al (c), O (d), Cu (e), C(f) and (g) digital photos of the pellet showing different sides. The Li metal anode was squeezed between electrolyte and copper current collector, as shown in Fig. 4g. F, Al, O were found to be distributed in the cathode, electrolyte, and anode. F and Al are present in the anode layer as well. To investigate the cross sections of the pellet, we cut the pellet using an ultrasonic knife. Al and F might have spread over the anode layer during the cutting process of the pellet. The presence of O in the anode layer could be due to the surface oxidation of Li metal.

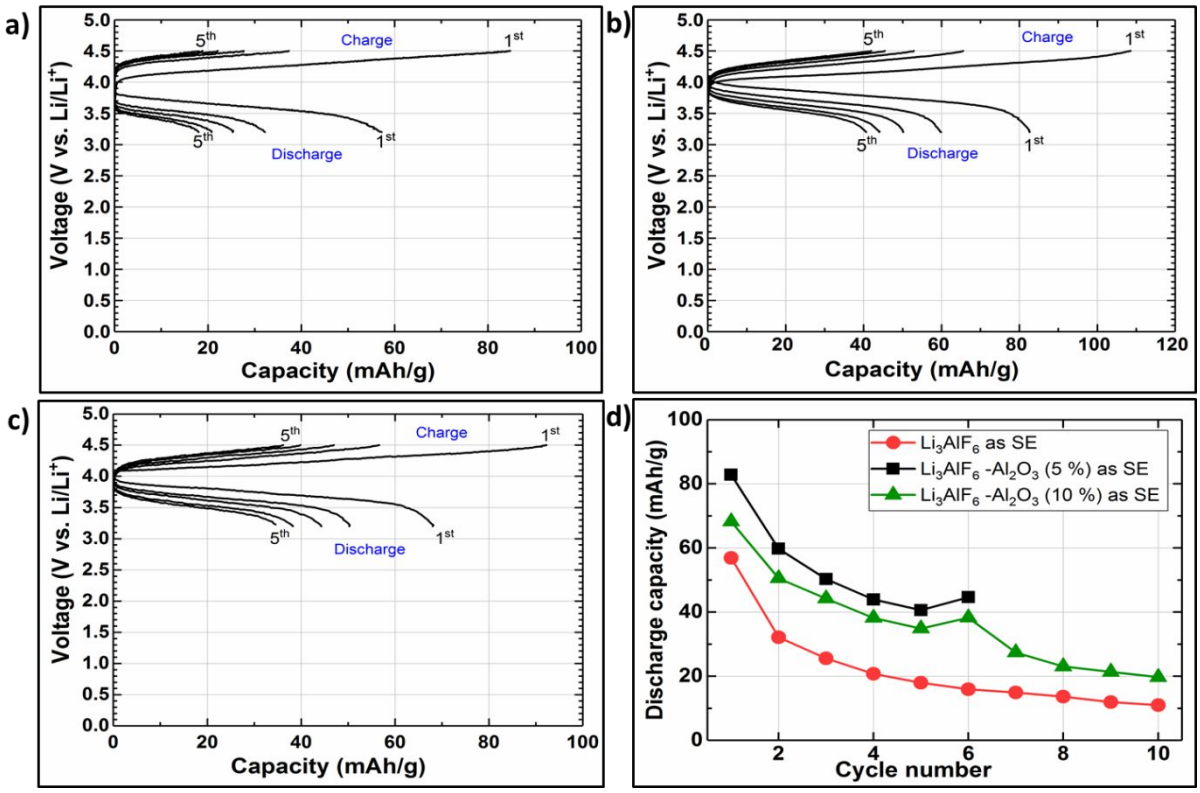

Figure 5 *charge/discharge profiles of a) Li/ β-Li_3AlF_6/$LiMn_2O_4$ b) Li/ β-Li_3AlF_6+Al_2O_3 (5%)/$LiMn_2O_4$, c) Li/ β-Li_3AlF_6+Al_2O_3 (10%)/$LiMn_2O_4$ cells and d) cycling behaviour of the corresponding cells.*

Fig. 5 shows the charge/discharge profiles of the Li/β-Li_3AlF_6/$LiMn_2O_4$ (Fig. 5a), Li/β-Li_3AlF_6+Al_2O_3(5%)/$LiMn_2O_4$ (Fig. 5b) and Li/ β-Li_3AlF_6+Al_2O_3(10%)/$LiMn_2O_4$ (Fig. 5c) cells together with their cycling behaviour (Fig. 5d). The cells were cycled in the voltage window of 3.2-4.5 V at 100 °C and at a current density of 26 μA cm^{-2}. The first charge/discharge capacities of the cells with β-Li_3AlF_6, β-Li_3AlF_6+Al_2O_3(5%) and β-Li_3AlF_6+Al_2O_3(10%) electrolytes were 85/57, 108/83, 92/68 mAh g^{-1}, respectively. In all cases, capacity faded rapidly during cycling. The reversible capacities of 18, 41, and 35 mAh g^{-1} were observed after five cycles in cells with β-Li_3AlF_6, β-

Li_3AlF_6+Al_2O_3(5%) and β-Li_3AlF_6+Al_2O_3(10%) electrolytes respectively. Further, the polarization between charge and discharge voltage is less in the cell with β-Li_3AlF_6+Al_2O_3(5%) electrolyte. The marginally better electrochemical performance of the cell with β-Li_3AlF_6+Al_2O_3(5%) electrolyte is due to the higher ionic conductivity of β-Li_3AlF_6+Al_2O_3(5%) compared to β-Li_3AlF_6, β-Li_3AlF_6+Al_2O_3(10%) electrolytes. However, the overall electrochemical performance of the cells was poor, which can be attributed to two factors. First, the ionic conductivity of the electrolytes was low, even at 100 °C (conductivity of β-Li_3AlF_6+Al_2O_3(5%) at 100 °C is $1.2x10^{-5}$ S cm^{-1}). Considering the large thickness of the electrolyte layer, this low ionic conductivity is not significant. Furthermore, $LiMn_2O_4$ is vulnerable to high-temperature cycling (100 °C). However, considering the desired electrolyte layer thickness of 10 to 20 μm for commercial solid-state batteries, the identification of fluoride-based electrolytes with ionic conductive in the range of 10^{-4} to 10^{-5} S cm^{-1} at RT would be promising for the future development of all solid-state lithium batteries.

Conclusions

In conclusion, our studies reveal the hidden potential of metal fluoride based solid-state electrolytes for all-solid-state batteries. We have demonstrated the viability of such metal fluoride based solid electrolytes with the aid of β-Li_3AlF_6 as solid electrolyte. We showed that the ionic conductivity of β-Li_3AlF_6 could be increased up to ten times by compositing with γ-Al_2O_3 (heterogeneous doping). Further, using DFT studies, we showed that Li possesses three-dimensional (3D) diffusion pathways in β-Li_3AlF_6. The performance of β-Li_3AlF_6 as a solid electrolyte was evaluated in an all solid-state lithium battery using $LiMn_2O_4$ as cathode and Li metal as anode materials. Though the electrochemical properties of the studied cells were poor, which is mainly due to the poor ionic conductance of the thick β-Li_3AlF_6 layer, the identification of fluoride-based electrolytes with better ionic conductivity can be promising for the future development of all solid-state lithium batteries.

ASSOCIATED CONTENT

Supporting Information (SI)

The Supporting Information is available free of charge on the ACS Publications website.

Supporting information is available on XRD, SEM, EIS and electrochemical studies.

AUTHOR INFORMATION

Corresponding Author

*E-mail: munnangi.reddy@kit.edu

ACKNOWLEDGMENTS

The authors would like to thank Mr. Tobias Braun for his assistance with SEM measurements. This work contributes to the research performed at CELEST (Center for Electrochemical Energy Storage Ulm-Karlsruhe).

METHODS

Synthesis of electrolyte and electrode materials

Materials synthesis, characterization, battery assembly, and testing of cells, were carried out under argon atmosphere. Electrolyte and electrode materials were prepared by mechanical milling. β-Li_3AlF_6 was synthesized by mechanical milling of LiF (Alfa Aesar, metal basis, 99.98%) and AlF_3 (Alfa Aesar, anhydrous, > 99%) at 600 rpm for 20h. Mechanical milling was performed using Fritsch, model Pulverisette 6, using ZrO_2 vial (80 ml) and balls (10 mm in diameter). A ball to powder ratio of 15:1 was used. β-Li_3AlF_6+Al_2O_3 composites were also made by mechanical milling. Before use, Al_2O_3 nanopowder (Sigma Aldrich, 13 nm, 99.8% trace metals basis) was heated for 2 h at 700 °C to remove any moisture. β-Li_3AlF_6 and Al_2O_3 composites were made with 2, 3, 5, 10 or 20 wt% alumina. Both powders were milled together at 300 rpm for 12h. $LiMn_2O_4$ was synthesized by high-temperature solid-state reaction. Li_2CO_3 and MnO_2 were mixed in stoichiometric ratio and heated at 650 °C for 12h

and further at 850 °C for 20h in an alumina crucible. The $LiMn_2O_4$ cathode composite was prepared by mixing active material $LiMn_2O_4$ (40 wt%), electrolyte (50 wt%) and carbon back (10 wt%) together at 100 rpm for 12 hrs.

Characterization

X-ray diffraction (XRD) analysis of the electrolyte and electrode composites was performed using a STOE STADI-P instrument with Cu-Kα source. Profile matching refinements were performed on the XRD patterns for cell average crystallite size calculation, using Langford's method with the FullProf software [31]. The morphology of the samples was investigated using high-resolution scanning electron microscopy (LEO 1550VP Field Emission SEM, Zeiss) equipped with an energy-dispersive spectrometer. An inert atmosphere transfer box was used in a few cases to avoid contact with the external environment.

Electrochemical Impedance Spectroscopy (EIS)

EIS spectra were recorded using a Zahner/IM6 device between 25 and 200 °C under Ar atmosphere. The EIS spectra were measured on pellets (7 mm diameter and ~1 mm thickness) pressed at 2 tons for 1 minute and sputtered with gold metal on both sides as ion blocking electrodes. EIS measurements were carried out over a frequency range from 1 MHz to 1 Hz, with a voltage amplitude of 10 mV. For a cylindrical pellet with a base area A, thickness d and resistance R the conductivity is given by

$$\sigma = \frac{d}{A \cdot R}$$

To get the resistance R, the obtained experimental data were plotted in a Nyquist plot, and the software Relaxis 3 was used to fit the data. For the coated cells of the solid electrolyte, a serially connected RQ-circuit with a single constant phase element (CPE) was chosen as a model.

Cell Fabrication and Electrochemical Testing

All solid-state battery pellets were fabricated by pressing Li (pressed on Cu), electrolytes and $LiMn_2O_4$ cathode composite together using a desktop press (Specac) inside an argon-filled glove box with water and oxygen contents below 0.1 ppm. The pellet was then transferred to a modified Swagelok type cell. Stainless steel discs were used as current collectors. Electrochemical testing of the cells was performed at 100 °C, using an Arbin battery tester (BT-2000) in galvanostatic mode. The cells were cycled in the voltage window of 3.2-4.5 V at a current density of 26 μA cm^{-2}. The specific capacities were calculated with respect to the weight of active material ($LiMn_2O_4$) in the cathode. For the CV measurements, β-Li_3AlF_6 or β-Li_3AlF_6+Al_2O_3 was pressed between Li and Al foil and scanned in the voltage window of -0.5-6.0 V at a temperature of 100 °C. The voltage scan rate used for CV measurements was 1 mV s^{-1}. Chronopotentiometry (CP) measurements were performed on symmetric Li/β-Li_3AlF_6/Li cells.

Computational Methods:

To theoretically investigate the β-Li_3AlF_6 phase we have conducted a density functional theory (DFT) study of Li diffusion in this compound, using the periodic DFT code VASP. For the description of the electron-ion interaction the projector-augmented wave (PAW) method was applied, while exchange and correlation were accounted for by the general gradient approximation (GGA) in the formulation of Perdew, Burke and Ernzerhof [32]. Spin-polarized calculations were conducted with a dense k-point mesh and a plane wave cutoff of 600 eV. The fully occupied β-Li_3AlF_6 structure was optimized with respect to lattice parameter and atomic positions. To determine the minimum energy path between different Li sites, the diffusion barriers were obtained by using the climbing image nudged elastic band method. By providing initial and final state of possible diffusion pathways, we have investigated a large number of different diffusion channels. Initial and final state configurations were obtained by introducing a vacancy on the initial and the final Li site and subsequent optimization of the atomic positions with the above described settings.

References:

1. Tarascon, J.-M.; Armand, M. Issues and challenges facing rechargeable lithium batteries. *Nature* **2001**, 414, 359–367.
2. Robinson, A. L.; Janek, J. Solid-state batteries enter EV fray. *MRS Bull.* **2014**, 39**,** 1046–1047.

3. Janek, J.; Zeier, W. G. A solid future for battery development. *Nat. Energy* **2016**, *1*, 16141.
4. Kerman, K.; Luntz, A.; Viswanathan, V.; Chiang, Y.-M.; Chen, Z. Practical Challenges Hindering the Development of Solid State Li Ion Batteries. *J. Electrochem. Soc.* **2017**, 164, A1731-A1744.
5. Richards, W. D.; Miara, L. J.; Wang, Y.; Kim, J. C.; Ceder, G. Interface Stability in Solid-State Batteries. *Chem. Mater.* **2016**, 8, 266-273.
6. Knauth, P. Inorganic Solid Li Ion Conductors: An Overview. *Solid State Ionics* **2009**, 180, 911–916.
7. Bachman, J. C.; Muy, S.; Grimaud, A.; Chang, H.-H.; Pour, N.; Lux, S. F.; Paschos, O.; Maglia, F.; Lupart, S.; Lamp, P.; Giordano, L.; Shao-Horn, Y. Inorganic Solid-State Electrolytes for Lithium Batteries: Mechanisms and Properties Governing Ion Conduction. *Chem. Rev.* **2016**, 116 (1), 140–162.
8. Thangadurai, V.; Weppner, W. Recent progress in solid oxide and lithium ion conducting electrolytes research. *Ionics* **2006**, 12 (1), 81-92.
9. Meesala, Y.; Jena, A.; Chang, H.; Liu, R.-S. Recent Advancements in Li-Ion Conductors for All-Solid-State Li-Ion Batteries. *ACS Energy Lett.,* **2017**, 2 (12), 2734–2751.
10. Zhang, Z.; Shao, Y.; Lotsch, B.; Hu, Y.-S.; Li, H.; Janek, J.; Nazar, L. F.; Nan, C.-W.; Maier, J.; Armand, M.; Chen, L. New horizons for inorganic solid state ion conductors. *Energy Environ. Sci.* **2018**, 11, 1945-1976.
11. Yu, C.; Ganapathy, S.; van Eck, E. R. H.; Wang, H.; Basak, S.; Li, Z.; Wagemaker, M. Accessing the bottleneck in all-solid state batteries, lithium-ion transport over the solid-electrolyte-electrode interface. *Nat. Commun.,* **2017**, 8 (1086), 1-9.
12. Stramare, S.; Thangadurai, V.; Weppner, W. Lithium lanthanum titanates: a review. *Chem. Mater.,* **2003**, 15 (21), 3974-3990.
13. Delmas, C.; Nadiri, A.; Soubeyroux, J. L. The nasicon-type titanium phosphates $ATi_2(PO_4)_3$ (A=Li, Na) as electrode materials. Solid State Ionics, 1988, 28-30, 419-423.
14. Liao, P.; Li, J.; Dahn, J. R. Lithium Intercalation in $LiFe_2F_6$ and $LiMgFeF_6$ Disordered Trirutile-Type Phases. *J. Electrochem Soc.* **2010**, 157, A355-A361.
15. Rongeat, C.; Reddy, M. A.; Witter, R.; Fichtner, M. Nanostructured Fluorite-Type Fluorides as Electrolytes for Fluoride Ion Batteries. *J. Phys. Chem. C* **2013**, 117, 4943−4950.
16. Rongeat, C.; Reddy, M. A.; Witter, R.; Fichtner, M. Solid Electrolytes for Fluoride Ion Batteries: Ionic Conductivity in Polycrystalline Tysonite-Type Fluorides. *ACS Appl. Mater. Interfaces* **2014**, 6, 2103-2110.
17. Lieser, G.; Drager, C.; Schroeder, M.; Indris, S.; de Biasi, L.; Gesswein, H.; Glatthaar, S.; Ehrenberg, H.; Binder, J. R. Sol-Gel Based Synthesis of LiNiFeF6 and Its Electrochemical Characterization. *J. Electrochem. Soc.* **2014**, 161, A1071-A1077.
18. Zhang, L.; Reddy, M. A.; Fichtner, M. Development of tysonite-type fluoride conducting thin film electrolytes for fluoride ion batteries. *Solid State Ionics* **2015**, 272, 39-44.
19. Xie, J.; Sendek, A. D.; Cubuk, E. D.; Zhang, X.; Lu, Z.; Gong, Y.; Wu, T.; Shi, F.; Liu, W.; Reed, E. J.; Cui, Y. Atomic Layer Deposition of Stable $LiAlF_4$ Lithium Ion Conductive Interfacial Layer for Stable Cathode Cycling. *ACS Nano* **2017**, 11 (7), 7019–7027.
20. Oi, T.; Miyauchi, K.; Uehara, K. Electrochromism of WO_3/$LiAlF_4$/LiIn Thin film over layers. *J. Appl. Phys.* **1982**, 53 (3), 1823–1823.
21. Liang, C. C. Conduction Characteristics of the Lithium Iodide-Aluminum Oxide Solid Electrolytes, *J. Electrochem. Soc.* **1973**, 120, 1289-1292.
22. Saito, Y.; Maier, J. Conductivity enhancement of CaF_2 by grain boundary activation with Lewis acids *Solid State Ionics* **1996**, 86-88, 581-584.
23. Li, J.; Ma, C.; Chi, M.; Liang, C.; Dudney, N. J. Solid Electrolyte: The Key for High-Voltage Lithium Batteries. *Adv. Energy Mater.* **2015**, 5 (4), 1401408.
24. Oi, T.; Miyauchi, K. Amorphous thin film ionic conductors of $mLiF.nAlF_3$. *Mater. Res. Bull.,* **1981**, 16, 1281-1289.
25. Esaka, T.; Okuyama, R.; Iwahara, H. Ionic conduction in sintered fluorocomplexes Li_mMF_6, M=Al, Ti. *Solid State Ionics* **1989**, 34, 201-205.
26. Miyazaki, R.; Maekawa, H. Li^+-Ion Conduction of Li_3AlF_6 Mechanically Milled with LiCl. *ECS Electrochem. Lett.,* **2012**, 1, A87-A89.
27. Garton, G.; Wanklyn, B. M. Polymorphism in Li_3AlF_6, *J. Inorg. Nucl. Chem.* **1965**, 27, 2466.
28. Tyagi, A. K.; Köhler, J. Preparation and rietveld refinement of the structure of beta-Li_3AlF_6. *Mater. Res. Bull.,* **1997**, 32, 1683–1689.

29. Han, X.; Gong, Y.; Fu, K.; He, X.; Hitz, G. T.; Dai, J.; Pearse, A.; Liu, B.; Wang, H.; Rubloff, G.; Mo, Y.; Thangadurai, V.; Wachsman, E. D. ;Hi, L. Negating interfacial impedance in garnet-based solid-state Li metal batteries. *Nat. Mater.,* **2017**, 16, 572–579.
30. Jung, S. C.; Han, Y.-K. How Do Li Atoms Pass through the Al_2O_3 Coating Layer during Lithiation in Li-ion Batteries? *J. Phy. Chem. Lett.,* **2013**, 4 (16), 2681-2685.
31. Langford, J. A rapid method for analysing the breadths of diffraction and spectral lines using the voigt function. *J. Appl. Crystallogr.* **1978**, 11, 10−14.
32. Perdew, J. P.; Burke, K.; Ernzerhof, M. Generalized Gradient Approximation Made Simple. *Phys. Rev. Lett.* **1997**, 77, 3865–3868.

TOC